SAXS in Inorganic and Bioinspired Research

Tomasz M. Stawski[1], Liane G. Benning
Cohen Biogeochemistry Laboratory, School of Earth and Environment, University of Leeds, Leeds, United Kingdom
[1]Corresponding author: e-mail address: t.m.stawski@leeds.ac.uk

Contents

Abstract

In situ and time-resolved structural information about emergent microstructures that progressively develop during the formation of inorganic or biologically mediated solid phases from solution is fundamental for understanding of the mechanisms driving complex precipitation reactions, for example, during biomineralization. In this brief chapter, we present the use of small- and wide-angle X-ray scattering (SAXS and WAXS) techniques and show how SAXS can be used to gather structural information on the nano-scale properties of the *de novo*-forming entities. We base the discussion on several worked examples of inorganic materials such as calcium carbonate, silica, and perovskite-type titanates.

1. INTRODUCTION

The making of bonds during the formation of inorganic or biologically mediated solid phases from solution usually follows a series of complex steps and pathways that most often depend on molecular-level reactions occurring at fluid–surface interfaces. *In situ* and time-resolved structural information about size, shape, crystallinity, and any mutual interaction between emergent microstructures that progressively develop during such processes provides us with the crucial building blocks to further our fundamental understanding of the kinetics, energetics, and mechanisms driving complex phase-forming reactions. The fact that the emergent species are often structurally poorly ordered, nanoparticulate and in many cases unstable dictates that ideally they must be characterized not just at length scales <100 nm but also as *in situ* as possible to avoid any artifacts due to sample handling, etc. Therefore, solution-based X-ray scattering methods are one of the most effective tools in studying nanostructured materials as they form in fluid media. In this brief chapter, we will discuss specifically the use of (ideally simultaneous) small- and wide-angle X-ray scattering (SAXS and WAXS) techniques and show how SAXS can be used to gather structural information on the nanoscale properties of the *de novo*-forming entities, whereas WAXS (basically X-ray diffraction) provides us with the atomic length-scale characterization information of the same reaction.

2. GENERAL CONSIDERATIONS: HOW DOES SAXS/WAXS WORK AND WHEN IT IS APPLICABLE?

Let us consider a sample that is either particulate or bicontinuous, that is, nonparticulate in nature but that has nanometer-range electronic density variations. Such variations could originate from homogenous colloidal particles of electronic density ρ that are dispersed in a matrix of a constant, but different, electronic density ρ_0 (e.g., a solvent). Equally, such variations could be due to presence of pores in a constant electronic density matrix or the coexistence of two continuous phases of different electronic densities but separated at a nanometer scale within a sample body (e.g., bicontinuous emulsions; Craievich, 2002; Glatter & Kratky, 1982; Guinier & Fournet, 1955; Stribeck, 2007). In all these cases, the difference in average electron density, $\Delta\rho$, leads to a "two-electron density system." $\Delta\rho$ will hereafter be referred to as the scattering contrast and $\Delta\rho \neq 0$ is a necessary condition for scattering to occur.

Applying this to SAXS experiments and combining it with a monochromatic collimated X-ray beam that passes through a sample that exhibits a scattering contrast, $\Delta\rho$, leads to the recording of the elastically scattered photons at very small angles. This is most often done using a 2D plate detector (Fig. 5.1A).

Overall, both small- and wide-angle scattering measurements can be performed either with conventional laboratory X-ray lamps or with synchrotron X-ray radiation. Depending on the measured angular ranges and light wavelengths, a SAXS pattern allows a series of structural parameters about the solid entities in a sample to be evaluated (e.g., size, size distribution, geometric shape, and agglomeration with dimensions typically 0.1–<500 nm; Bras, 1998; Craievich, 2002; Rieckel, Burghammer, & Müller, 2000; Stribeck, 2007). The resulting recorded scattering intensity is conventionally plotted as the function of the modulus of the scattering vector $\mathbf{q}$ (nm^{-1}), which is related to the scattering angle 2θ and the wavelength λ (nm) of the incident beam via (Eq. 5.1)

$$q = (4\pi/\lambda)\sin\theta \qquad (5.1)$$

where q is the modulus (magnitude) of $\mathbf{q}$.

A representative 2D scattering pattern of a sample containing agglomerated particles in solution is shown in Fig. 5.1B. It is worth mentioning that in order to extract the maximum information about the in-sample-contained structures, it is paramount that the used q-range must be adjusted before each SAXS experiment to match as best as possible the expected range of sizes of the investigated structural features. This is the necessary practical condition for a successful SAXS experiment. This condition is important because if the minimum expected particle size is denoted by D_{min} and the maximum by D_{max}, this leads to the q-range needing to be set to fit $q_{min} = \pi/D_{max} < q < q_{max} = \pi/D_{min}$ (Glatter & Kratky, 1982). For a q-range defined in such a way, the scattering data will contain the full information for all particles in the size range between D_{min} and D_{max}. However, if a scattering pattern contains information from semiperiodic (e.g., correlated or *pseudo*crystalline) structures, the q-range is also dependent on the maximum and minimum interparticle distances, d_{max} and d_{min}, with $q_{min} = 2\pi/d_{max} < q < q_{max} = 2\pi/d_{min}$, as defined by the Bragg equation. These parameters are obviously dependent not only on the wavelength of the incident X-ray beam but also on the sample-to-detector distance, the area of the 2D detector, and the position of the beam on the detector (beam-stop position; e.g., placing a beam stop in the corner of the detector instead of the
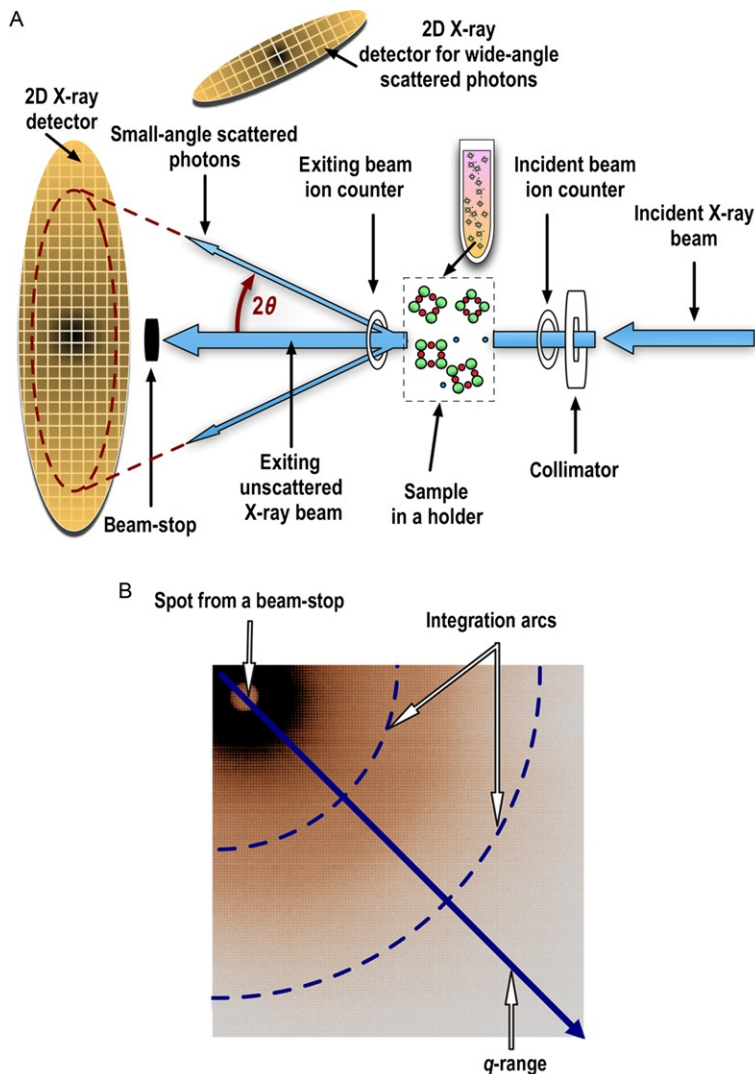
Figure 5.1 (A) Scheme of the typical SAXS/WAXS experiment; (B) example of a scattering pattern from a sample containing agglomerated particles in solution recorded with a 2D SAXS detector. Some of the elements relevant for the data-reduction steps explained in Section 4 are marked in the figure.

middle allows for more than doubling of the measured q-range; Fig. 5.1B). The actual measured q-range in absolute units (nm^{-1} or $Å^{-1}$) with respect to pixel/channel positions on any detector needs to be established, each time, by means of a standard, that is, a chemical compound of known structure

exhibiting Bragg diffraction peaks in the measured low-angular range. For instance, silver behenate ($d_{max} = 5.8380(3)$ nm; Huang, Toraya, Blanton, & Wu, 1993) or wet rat tail collagen ($d_{max} = $ ca. 67 nm; Fratzl et al., 1997) is most often used for this purpose depending on the investigated q-range.

SAXS instruments are often complemented with WAXS detectors (Fig. 5.1A). These record those photons scattered at higher angles, hence, extending the q-range to higher magnitudes of the scattering vector. The investigated system is targeting not just poorly ordered nanostructures but possibly also particles with emerging and developing crystalline or nanocrystalline properties. These higher-angle scatterers would produce a diffraction pattern, which will be recorded in the WAXS regime. Such patterns complement the SAXS data and give us quantitative information about the internal structure of forming ordered entities.

3. WHAT HAPPENS IN A SOLUTION WHEN IONS MEET AND HOW DO WE QUANTIFY IT?

In this section, we very briefly review how amorphous and crystalline inorganic materials are known to form from solutions. It is not our aim to discuss these complex processes in detail nor will we address the thermodynamics or detailed kinetic aspects related to such reactions, but we will focus merely on a simplified structural description and only partially address basic kinetic aspects. This introduction is necessary for a better understanding of not only the advantages but also limitations of SAXS for solution-based particle nucleation and growth investigations and to indicate where complementary and/or alternative methods should be/need to be used to derive quantitative data about such reactions. In every scientific study, it should be always clear that no single method alone ever provides a conclusive answer to any scientific question and that in all cases multiple and complementary analytic and experimental approaches need to be employed to achieve a rigorous scientific result.

3.1. Formation of inorganic materials from solutions

The growth of any solid material from solution is essentially an evolutionary process in which at different stages of growth, species of various shapes, size, and internal structure form and further convert into a final product (amorphous colloidal gel, crystal, etc.).

In the case of nucleation and crystallization phenomena occurring in solutions, relevant but not exclusive to (bio)mineralization, two descriptions

are used: the classical nucleation theory (CNT) often applied universally as a starting point for further discussions (Becker & Döring, 1935; Benning & Waychunas, 2007; Volmer & Weber, 1925) and the relatively novel prenucleation concept developed and confirmed for calcium carbonate and calcium phosphate (Dey et al., 2010; Gebauer & Cölfen, 2011; Gebauer, Völkel, & Cölfen, 2008; Fig. 5.2A). In both cases, the formation of a new entity starts with a change in supersaturation of a reacting solution of dissolved species that leads progressively, fast or slow, to the coalescence of a first "solid" entity. From this initial entity, the reaction can follow many pathways, but ultimately, the reaction chain completes with the formation of a stable crystal. From the structural point of view, CNT assumes that elementary nuclei form in the supersaturated solution and that this proceeds further through attachment of basic monomers (atoms, ions, and molecules) to this newly formed entity (Benning & Waychunas, 2007). Structurally, this newly formed elementary nucleus is indistinguishable from that of the intended bulk material. However, these smaller nuclei are most often thermodynamically unstable and dissolve and thus the material grows from nuclei of a certain critical size (critical nucleus), leading eventually to the formation of the so-called primary particle. CNT has been used universally in the last few decades, and it is still applicable in many systems. For example, just recently, CNT has been confirmed for the nucleation and growth of magnetite crystals (Fe_3O_4), which have been shown to form via a basic-pH coprecipitation route, describable within CNT (Baumgartner et al., 2013). On the other hand, in the case of $CaCO_3$, Gebauer and co-workers (Gebauer & Cölfen, 2011; Gebauer et al., 2008) proposed an alternative mechanism (Fig. 5.2A) that implies that within a supersaturated solution, the first entities that form are stable prenucleation clusters. Only in subsequent stages do these prenucleation clusters aggregate into larger amorphous particles, which can further agglomerate, coalesce, and eventually covert via various pathways into a crystalline phase. This also implies that any species forming before the nucleation and growth of the crystal must be structurally different from the final material, yet they suggest that likely there is a structural "memory" effect that affects these reactions. For example, in the $CaCO_3$ system, depending on physicochemical conditions at which the experiments are carried out, the prenucleation clusters, and the subsequently formed amorphous calcium carbonate (ACC), seem to have a structural "memory" that leads to ACC that is structurally more alike with the final crystalline entity that it will transform into (e.g., ACC with a vaterite-, calcite-, or aragonite-like protostructure; Bots, Benning, Rodriguez-Blanco,
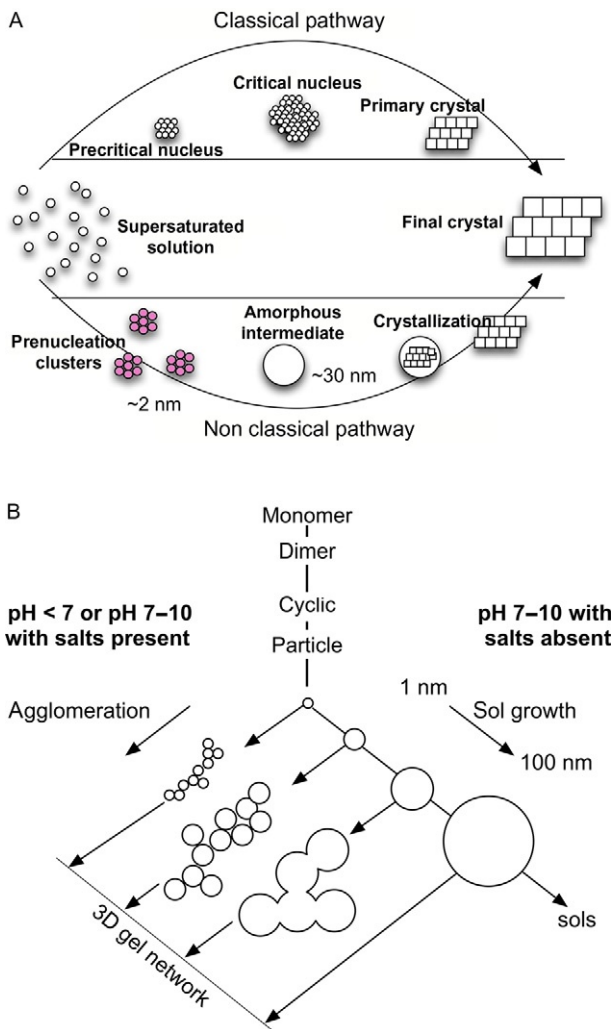
Figure 5.2 (A) Classical and nonclassical pathways describing growth of the crystalline materials from solutions. (B) Scheme representing the evolution of aqueous silica system from monomers to developed sols and gels, in relation with reaction conditions. *Panel (A) is based on Meldrum and Sear (2008) and Gebauer and Cölfen (2011), and panel (B) is based on Iler (1979).*

Roncai-Herrero, & Shaw, 2012; Gebauer & Cölfen, 2011). These matters are still in debate and discussion as the reactions are fairly complex, but scattering can help elucidate some of the still open questions. Naturally, these descriptions of complex reactions have been in this chapter highly simplified. Many reviews

that discuss the pathways of the formation of ACC in pure or biomimetic/ biomineralization scenarios in detail are available (e.g., Gower, 2008; Meldrum & Cölfen, 2008). However, what is important for this discussion is the fact that on the pathway between the solution stage and the final (most often crystalline) stable end product, emergent discrete nanostructures form. The morphology and rate of development of these nanostructures depends on physical and chemical parameters of the evolving system, and any small modification in any of the parameters at any stage in the process has invariably nonnegligible implications for any of the consequent steps. For such emerging properties, SAXS is an ideal technique as it can provide information at fast timescales and also at the spatial scale needed to observe these entities (provided that enough particles are present in the X-ray-illuminated volume of fluid).

Another example of emerging entities from supersaturated aqueous solutions is the evolution of aqueous silica from solution. The SiO_2 system is ideal to illustrate the connection between reaction conditions and development of solid amorphous silica nanoparticles (Fig. 5.2B; Brinker & Scherer, 1990; Iler, 1979). In aqueous solution and depending on conditions, silica, $Si(OH)_4$, can polymerize via various steps: (1) $Si(OH)_4$ monomers coalesce into particles through dimer-cluster and cyclic-cluster stages; (2) in acidic solutions or in the presence of flocculating salts, sub–10 nm particles aggregate into networks, which form a gel; or (3) in basic solutions with salts absent, the growth of homogenous sol particles occurs, with particle sizes reaching 100 nm (Fig. 5.2B; Brinker & Scherer, 1990; Iler, 1979). These systems have been widely investigated mainly due to not only the technological, geochemical, and biological significance of silica but also the impeded reactivity of silicon-carrying precursors in comparison with transition metal analogues, providing with a good study model system for metal oxide colloid science in general (Brinker & Scherer, 1990; Wright & Sommerdijk, 2001). Aqueous and nanoparticulate silica has many technological applications and is industrially directly obtained in its amorphous form most often from alkoxide precursors. The use of metal–organic starting materials makes it simpler to link the properties of sols with the properties of expected solid final products. For such studies, the use of SAXS is ideal because in the alkoxide silica system, homogenous and most often relatively monodispersed particles form from solution which is favorable in many industrial applications. However, such organically produced SiO_2 particles have little to say about how silica, the most abundant compound in the Earth's crust, forms in a natural—nonindustrial—setting. We will discuss

later (Section 5.2) how this has been the focus of recent studies (Tobler & Benning, 2013; Tobler, Shaw, & Benning, 2009) that employed synchrotron–based X-ray scattering to quantify the nucleation and growth of silica nanoparticles from inorganic solutions, mimicking natural processes.

3.2. The suitability of synchrotron-based scattering methods

Synchrotron-based SAXS in particular and WAXS in some cases are powerful tools enabling extraction of structural information about emergent properties of new phases forming from and in solutions because of the following:

- From its very principle requiring the occurrence of the scattering contrast, scattering methods are sensitive to the presence of particulates suspended in solution. Furthermore, ideally, the growing phases have relatively high electron density in comparison with the solvent, and thus, the scattering contrast is high.

- Scattering methods enable *in situ* and time-resolved measurements of an evolving system in which particles are in a constantly changing quasiequilibrium with the reacting medium; in some cases, measurements under other physical conditions can also be achieved, for example, nonequilibrium physical drying (Stawski, Veldhuis, Castricum, et al., 2011; Stawski et al., 2011b).

- The emergent species range in size from <1 nm to a few micrometer, with length scales at the most crucial prenucleation, nucleation, and growth phases contained at sub-200 nm. This is the length scale ideally adjusted for X-ray scattering experiments.

- From the kinetic point of view, any reaction that is followed using scattering needs to ideally occur at resolvable timescales; these can be sub-100 ms to 1 min and/or be up to many hours (Bots et al., 2012). For instance, as mentioned earlier, crystalline $CaCO_3$ phases form via ACC precursors (Meldrum & Cölfen, 2008). ACC precipitates from supersaturated solutions at ambient conditions as nanoparticles within seconds (Rodriguez-Blanco, Shaw, & Benning, 2008). *In situ* and time-resolved scattering and diffraction studies (Bots et al., 2012; Rodriguez-Blanco, Shaw, & Benning, 2011) showed that in purely inorganic systems, ACC transforms to crystalline $CaCO_3$ polymorphs within minutes to hours and that nucleation, growth, and transformation mechanisms and kinetics depend on variations in saturation states, temperature, pH, or the presence or absence of foreign ions (Loste, Wilson, Seshadri, & Medrum, 2003; Meldrum &

Cölfen, 2008). However, so far, the extremely low concentration of prenucleation clusters in a supersaturated calcium carbonate solution and the invariably small electron density contrasts between these clusters and the reacting solutions have precluded the use of scattering methods and the characterization of the clusters *in situ*. The data about their existence are primarily derived from titration and analytic centrifugation studies (Gebauer & Cölfen, 2011; Gebauer et al., 2008).

- In SAXS experiments, only a small fraction of the incident X-ray beam is scattered by the sample; however, the required time resolution and scattering intensity are achievable with the use of the high brightness and high flux of synchrotron-based SAXS. Modern pixel array detectors, such as Dectris Pilatus series (Mueller, Wang, & Schulze-Briese, 2012), may be able to provide the time resolution necessary to monitor cluster formation and all transformations reactions over the desired range of length scales, with high-quality data now possible to be acquired in sub-50 ms time-resolved snapshots. On the other hand, time-resolved experiments on systems of low electron density contrast cannot be practically carried out with SAXS instruments using conventional X-ray sources (laboratory SAXS). The required data acquisition time per snapshot with acceptable signal-to-noise ratio reaches many minutes or hours, depending on the scattering contrast and the size of nanostructures. However, it should be pointed out that the laboratory SAXS instruments are also improved constantly in terms of X-ray collimation quality and detector sensitivity and resolution. For instance, recently, the formation of gold clusters (high-scattering contrast system) was followed with time resolution of sub-50 ms using a conventional, laboratory-based SAXS system (Polte et al., 2010).
- The development of crystalline structures of an emergent inorganic nanostructure is not measureable within the q-range recorded by SAXS, unless the developing ordered morphologies show diffraction peaks at low angles like, for example, metal–organic transition phases (Stawski, Veldhuis, Castricum, et al., 2011). This is clearly a hardware limitation related to the very physical area of the detector, but this can be partially overcome by using an auxiliary WAXS detector.
- WAXS is a diffraction method at very high q, which is ideally suited to extract information about the internal structure of the emergent phases, kinetics and energetics of their growth, and basic phase identification. This is valid provided that the phases are crystalline and that the number of particles within the scattering volume is sufficient for the diffraction

pattern to be recorded with any reasonable signal-to-noise ratio. WAXS methods have been used in the last two decades intensively in many inorganic systems to quantify the crystallization mechanisms, kinetics, and energetics of various systems with important biological and/or geochemical implications. For example, in highly anoxic systems, the solution-based crystallization of preformed, poorly ordered iron sulfide (mackinawite, nominal FeS) has been shown to, depending on redox conditions and additives, follow various pathways (Cahill, Benning, Barnes, & Parise, 2000). Under highly reducing conditions, mackinawite transforms first to a highly magnetic and Fe^{2+}/Fe^{3+}-bearing intermediate, greigite (Fe_3S_4, Hunger & Benning, 2007), which ultimately recrystallized and leads to the formation of the geologically stable pyrite (FeS_2). Similarly, *in situ* and time-resolved WAXS combined with electrochemical measurements have been recently used (Ahmed et al., 2010) to quantify in detail the formation pathways and mechanisms of green rust sulfate, a layered double-hydroxide phase with the capacity to reduce a range of inorganic and organic species. Finally, combining *in situ* crystallization with element-partitioning measurements in aqueous solutions, the formation and intertransformation of important iron-bearing phases (ferrihydrite to goethite and hematite, Davidson, Shaw, & Benning, 2008 or ferrihydrite to magnetite, Sumoondur, Shaw, Ahmed, & Benning, 2008) in the absence or presence of various toxic compounds (Vu, Shaw, Brinza, & Benning, 2010) have been quantified using WAXS and other *in situ* and time-resolved X-ray diffraction methods. Elucidating the mechanisms, kinetics, and energetics of these reactions helps understand the fate of toxic compounds in various natural and anthropogenically modified environments and this knowledge plays a crucial role in guiding remediation efforts in contaminated settings.

Thus, it is clear that WAXS in combination with SAXS is ideally suited to mark both the onset of transition between the solution and the amorphous stages and the transitions between the amorphous and crystalline stages in any reaction and that the *in situ* and real-time capabilities combined with special experimental settings that they offer can and are more and more used to better understand a plethora of industrial and natural processes.

4. SAXS DATA PROCESSING AND INTERPRETATION

In this section, we present the very basics of scattering data processing and interpretation. We do not explicitly describe WAXS data interpretation

since diffraction methods are well established and covered in the literature. However, what we summarize here is only the basic theory of scattering and as such this brief description should be treated accordingly.

4.1. Data treatment

If we consider the case of particles in a solution, the recorded scattering pattern is isotropic because nanometer-range electronic density variations are randomly oriented with respect to each other and the incident beam. In such a case, a 2D scattering pattern is transformed to a 1D scattering curve in a data–reduction step (Craievich, 2002; Glatter & Kratky, 1982; Guinier & Fournet, 1955; Stribeck, 2007). The as-measured intensity values need to be corrected for detector alinearities, fluctuating X-ray beam intensity using the exiting beam ion counter (Fig. 5.2A)—and background scattering. The scattering curve of interest is subsequently obtained by integration of the measured intensities along the arcs having an origin at $q=0$ (center of the beam spot on the detector, hence, $q=0$ is extrapolated from the calibration data), having radii corresponding to consequent discrete q values and lengths defined by the shape of the detector (Fig. 5.2B) (Pauw, 2013).

4.2. Data interpretation

In the case of particles forming from a supersaturated solution, SAXS can be used to derive information about the size and shape of individual particles, their interactions, and their polydispersity, number density (concentration), or molecular weight. However, because these parameters are in fact mutually coupled, only certain combinations of structural elements can be obtained from a single system measured at a given q-range. That means that either certain simplifications concerning the structure need to be made or the sample has to be prepared and measured in a way that enables the exclusion of some of the "unwanted" factors (e.g., interparticle interactions can be avoided by using dilute systems). Similarly, missing data on specific parameters (e.g., shape of particles, polydispersity, and aggregation) must be obtained by other spectroscopic (e.g., vibrational, X-ray absorption, and nuclear magnetic resonance) or imaging methods (e.g., high-resolution scanning or transmission electron microscopy). These limitations result from the very physics of scattering, as will be described further later.

    In general, the scattering amplitude $F(\mathbf{q})$ from an individual scattering primary particle that is embedded in a homogenous matrix can be approximated by Eq. (5.2) (Feigin & Svergun, 1987; Glatter & Kratky, 1982;

Guinier & Fournet, 1955; Vachette & Svergun, 2000). In this equation, it is assumed that in a given direction, only the scattering contrast $\Delta\rho(\mathbf{r})$ would be contributing to the scattering intensity. This direction is defined by the scattering vector $\mathbf{q}$ representing the electron density dependent on the position vector $\mathbf{r}$:

$$F(\mathbf{q}) = \int_V \Delta\rho(\mathbf{r})e^{-i\mathbf{q}\cdot\mathbf{r}}d\mathbf{r} \tag{5.2}$$

Hence, the scattered intensity of a single object, I_I, in the direction defined by a scattering vector is expressed by Eq. (5.3), where F^* is the complex conjugate of F:

$$I_I(\mathbf{q}) = F(\mathbf{q})F^*(\mathbf{q}) = \int_V\int_V \Delta\rho(\mathbf{r})\Delta\rho(\mathbf{r}')e^{-i\mathbf{q}\cdot(\mathbf{r}-\mathbf{r}')}d\mathbf{r}d\mathbf{r}' \tag{5.3}$$

For our purposes, we only consider (i) an isotropic system (hence describable by scalars q and r) of identical particles and a (ii) system showing no long-distance order (it is "dilute"). For a collection of identical non-interacting particles of particle volume V, number N embedded in the homogenous matrix so that scattering contrast is $\Delta\rho$, the total scattering intensity $I(q)$ can be expressed as

$$I(q) = N\cdot I_I(q) = N(\Delta\rho)^2 V\cdot 4\pi\int_0^{D_{\max}} r^2\gamma(r)\frac{\sin(qr)}{qr}dr \tag{5.4}$$

where $D_{\max}$ denotes a maximum dimension within the scattering object and $\gamma(r)$ is known as the correlation function (Feigin & Svergun, 1987; Glatter, 1977; Glatter & Kratky, 1982; Guinier & Fournet, 1955; Vachette & Svergun, 2000). From this equation, we can derive the fact that the scattering intensity at $q=0$—termed $I(0)$—must be equal to $N(\Delta\rho)^2 V^2$.

To simplify matters, more commonly, instead of the correlation function, $p(r) = \gamma(r)r^2$ is used. This is referred to as a pair (distance) distribution function and $p(r)$ is related to the electron density contrast through Eq. (5.5).

$$p(r) = \gamma(r)r^2 = r^2\left\langle\int_V \Delta\rho(\mathbf{r})\Delta\rho(\mathbf{r}')\right\rangle_\Omega \tag{5.5}$$

where $\langle\rangle_\Omega$ denotes spherical averaging and Ω is a solid angle in the reciprocal space. $p(r)$ contains information on the complex shape and the structure of the scattering object. For many cases, it can be retrieved from the scattering intensity, as, for example, in the case of scattering from dilute solutions of

proteins (Feigin & Svergun, 1987; Putnam, Hammel, Hura, & Tainer, 2007; Vachette & Svergun, 2000). Overall, the value for $p(r)$ relates to $I(q)$ through an inverse Fourier transform:

$$p(r) = \frac{1}{2\pi^2} \int_0^\infty qrI(q)\sin(qr)\,\mathrm{d}q \qquad (5.6)$$

By finding $p(r)$, one can extract structural information from scattering objects of complicated shapes, because the pair distribution function (PDF) plot is essentially a histogram of all distances within a particle up to $D_{\max}$. This is valid provided that the considered system is monodisperse and dilute, as is often the case in proteins in solution (naturally depending on sample preparation). Equation (5.6) implies that $I(q)$ is measured at the infinite q-range and furthermore assumes a continuous nature of $I(q)$. However, these two conditions cannot be fulfilled in practice, and a direct Fourier transform of measured intensities often yields unreliable results (Glatter & Kratky, 1982). Instead, $p(r)$ is usually obtained through an indirect Fourier transform method (Glatter, 1977, 1981; Glatter & Kratky, 1982) that is usually implemented via software packages such as GNOM (Svergun, 1992) or GIFT (Brunner-Popela & Glatter, 1997).

It has to be noted, however, that $F(q)$ is also referred to as the amplitude of the scattering form factor, $P(q) = F^2(q)$. In the case of many known and classical geometric shapes (spheres, shells, cylindrical objects, Gaussian chains, etc.), the mathematical expressions for the form factors $P(q)$ are relatively easy to derive analytically and are available readily in the literature (Feigin & Svergun, 1987; Pedersen, 1997). For example, scattering from a collection of noninteracting, monodisperse homogenous spheres of radii R is expressed by Eq. (5.7), which is derived directly from Eq. (5.3), assuming an isotropic system and assuming $\Delta\rho(\mathbf{r}) = \Delta\rho$ for $\mathbf{r}$ inside the particle and $\Delta\rho(\mathbf{r}) = 0$ for $\mathbf{r}$ outside the particle:

$$I(q) = N(\Delta\rho)^2 V^2 P(q) = N(\Delta\rho)^2 V^2 \left(3\frac{\sin(qR) - qR\cos(qR)}{q^3R^3}\right)^2 \quad (5.7)$$

However, for changes in shape or other morphological parameters during a reaction, this is often far from trivial. We can apply certain approximations when evaluating SAXS data in order to obtain information about sizes and basic structural characteristics of the investigated species. For instance, for a dilute system of scattering particulate features, a shape-independent radius of gyration, R_g, can be found through applying the Guinier

approximation to the form factor, $P(q)$ (Guinier & Fournet, 1955). This is only valid, however, for $qR_g < 1$. Then, the scattering intensity is given by

$$I(q) = N(\Delta\rho)^2 V^2 \exp\left(\frac{-q^2 R_g^2}{3}\right) \tag{5.8}$$

Provided that the particles are sufficiently monodisperse, it is important to note that Eq. (5.8) is independent of the actual shape of the scattering features in the applicable q-range. In addition, a further generalization of the Guinier approximation to highly elongated and plate-like particles allows us to discriminate these geometries and obtain basic information on some of the characteristic dimensions, for example, cross-sectional radius of gyration of elongated particles (Feigin & Svergun, 1987; Glatter & Kratky, 1982; Guinier & Fournet, 1955).

If we aim to also include interparticle correlations in our scattering data evaluations, we can do that by taking into account Eqs. (5.1)–(5.5) and denoting that $P(q) = F^2(q)$. Thus, we can introduce interparticle spatial correlations by implementing a structure factor under the assumption that these correlations have an isotropic character:

$$I(q) = N(\Delta\rho)^2 V^2 P(q) S(q) \tag{5.9}$$

In this equation, $S(q)$ represents a structure factor term describing the mutual arrangement of primary particles of a given form factor, $P(q)$, within the measured sample volume of nondiluted systems. $S(q)$ takes into account any scattering interferences from different species due to any interactions between particles. Such interactions include Coulomb repulsion–attraction phenomena, aggregation and clustering effects, or other spatial correlations within the system. Hence, $S(q)$ provides additional geometric information, and this can be used indirectly to extract information about the dynamic processes and physicochemical interactions between the particles. In analogy to Eq. (5.4), we can express the structure factor $S(q)$ of an isotropic system through a correlation function. For the sake of clarity, this correlation function is denoted as $g(r)$ in Eq. (5.10) (Glatter & Kratky, 1982; Guinier & Fournet, 1955; Pedersen, 1997; Squires, 1978):

$$S(q) = 1 + 4\pi n \int_0^\infty [g(r) - 1] r^2 \frac{\sin(qr)}{qr} \, dr \tag{5.10}$$

where n denotes the number density of particles.

For dilute system of noninteracting particles, $S(q)=1$. Please note that in the formalism, $\gamma(r)$ discussed in Eqs. (5.4) and (5.5) is related to the internal structure of the individual scattering primary particles, whereas the $g(r)$ introduced earlier in Eq. (5.10) is related to the arrangement of the primary particles in space. Similarly to $\gamma(r)$ (and $p(r)$), $g(r)$ can under certain circumstances be extracted from the scattering data by reverse Fourier transform. Furthermore, one may include polydispersity, assuming different types of distributions, variable types of averaging (intensity, number, and weight), and assumptions about whether polydispersity is related to primary particles or structures formed by primary particles (e.g., whether it is related to $P(q)$ or $S(q)$; Pedersen, 1997).

It should now be clear from the description earlier that the evolution of inorganic solution-based nanostructures in the prenucleation phase and during the various stages of nucleation, aggregation, and/or growth/crystallization involves the formation of particles of certain sizes and shapes and that these change with time. Furthermore, any of the various stages in a whole reaction can involve processes of agglomeration and coalescence. Hence, the direct extraction of values for either $p(r)$ or $g(r)$ from any set of scattering data is difficult and possible only in a limited number of cases because of the following:

1. In order to extract complete information on the form factor, $P(q)$ (and $p(r)$), the scattering system must be monodisperse and dilute so that either $S(q)=1$ or $S(q)$ must be explicitly known from other measurements or alternatively convincingly assumed or deduced (Brunner-Popela & Glatter, 1997). In order to account for polydispersity of $P(q)$, and extract information about the distribution, one needs to know (or assume) the form of monodisperse $P(q)$.

2. In order to extract high-resolution information about the structure factor $S(q)$ (and $g(r)$), the form factor must be known or assumed, or for the considered q-range, the interparticle interactions need to occur on a length scale large enough to assume $P(q)=1$. In order to account for polydispersity of $S(q)$ and extract information about the distribution, one needs to know (or assume) the form of monodisperse $S(q)$.

3. Importantly, both $P(q)$ and $S(q)$ contain relevant information characterizing an evolving system. For instance, dilution to the point where $S(q)=1$ would mean practically quenching the process and altering the investigated system. Therefore, in the case of complex multistep-formed materials, the behavior of $I(q)$ is usually modeled assuming that $P(q)$ can be represented through simple geometric shapes (Glatter & Kratky, 1982; Pedersen, 1997). Similarly, this applies to $S(q)$, which is

usually modeled within specifically proposed structural arrangements and interactions (hard spheres, sticky hard spheres, fractal aggregates, etc.; Freltoft, Kjems, & Sinha, 1986; Kinning & Thomas, 1984; Pedersen, 1997; Sorensen, 2001; Teixeira, 1988).

A more detailed description and overview of the mathematical functions used to express various form and structure factors can be found in Pedersen (1997). Once derived, the so-obtained mathematical models can then be fitted to experimental data leading to an evaluation of parameter values that will characterize the investigated sample. Clearly, such an approach is often limited by the availability of existing models and their physical validity. Nevertheless, it has proven to be useful in providing information on the microstructure of such inorganic systems. To point a few, we mention here silica (Besselink, Stawski, Castricum, & ten Elshof, 2013; Freltoft et al., 1986; Teixeira, 1988), titania (Jalava et al., 2000; Kamiyama, Mikami, & Suzuki, 1992), zirconia (Riello, Minesso, Craievich, & Benedetti, 2003; Stawski et al., 2012), colloidal precursors for perovskite-type ceramics (Stawski et al., 2011a,2011b, 2012), sodium hydrous sulfate (Brand, Scarlett, Grey, Knott, & Kirby, 2013), or calcium carbonate (Bolze et al., 2002; Pontoni, Bolze, Dingenouts, Narayanan, & Ballauff, 2003).

Finally, it has to be mentioned that after the arduous stages of data processing and handling, the next step of data interpretation constitutes an equally nontrivial element when it comes to SAXS measurements. Additionally, because conventional SAXS is an electron density contrast-based method, it does not allow extracting chemical (compositional) information. Therefore, other auxiliary methods must be used to support findings obtained by SAXS. These would include, among others, element-specific anomalous (resonant) A-SAXS; small-angle neutron scattering and contrast matching; wide-angle X-ray scattering, that is, diffraction (WAXS) and atomic PDF analysis; X-ray absorption spectroscopy; various vibrational spectroscopic analyses; and natural hard and soft X-ray and electron microscopic approaches combined with related electron energy loss and energy dispersive spectroscopies and electron diffraction.

5. CASE STUDIES

5.1. Formation and growth of amorphous CaCO$_3$ and its crystallization

For the research community working in the field of biomineralization, investigations about the mechanisms controlling the precipitation of CaCO$_3$

from supersaturated solutions constitute a key aspect of research. However, it was only in the last 10 years, once time–resolved SAXS/WAXS was successfully applied for the first time to study these processes (Bolze et al., 2002), and that advances could be made. In the considered experiments, calcium carbonate was precipitated from aqueous solution of $CaCl_2 \cdot 2H_2O$ and Na_2CO_3 mixed using a stopped–flow device. By combining synchrotron-based SAXS data acquisition with a fast stopped–flow injection and mixing system, Bolze et al. (2002) were able to achieve time resolution of sub–100 ms and this allowed them to follow the nucleation and growth reaction through the changes in SAXS patterns for many minutes (Fig. 5.3). They
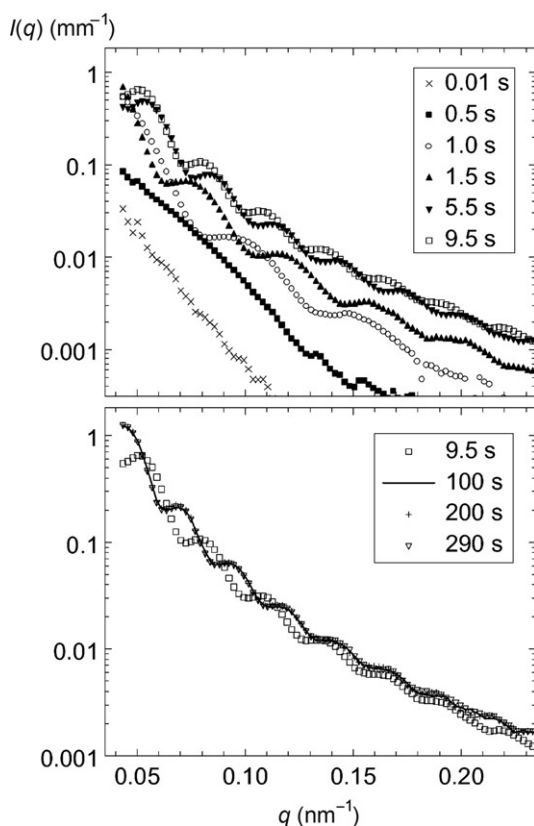
Figure 5.3 Time-resolved SAXS data measured after rapidly mixing aqueous solutions of $CaCl_2$ and Na_2CO_3 in a stopped-flow apparatus. After a short induction period of less than 500 ms, the scattering patterns exhibit marked oscillations. Particle growth is evidenced from the increase in the oscillation frequency and the concomitant increase of the intensity. *Printed with permission from Bolze et al. (2002). Copyright 2002 American Chemical Society.*

found that the developing particles were describable within the polydisperse spherical form factor of very narrow distribution but that they had diameters up to ca. 270 nm and the polydispersity was decreasing with the increasing size of the spheres. Their results also showed that the forming particles were amorphous in nature, which was further confirmed (Pontoni et al., 2003) by the lack of diffraction peaks in the simultaneously collected WAXS patterns. The formed ACC particles were found to remain "stable" in solution as isolated nonagglomerated entities for the measured time of 5 min. This conclusion was derived from data collected over a q-range extended to low values of the scattering vector, where no increase in $I(q)$ was observed and the assumption that such an increase would normally be attributable to the presence of agglomerates. Furthermore, the authors showed that after a short nucleation period, the number density of the growing spheres remained constant. From the evaluation of the absolute scattering intensities, the particle mass density was determined to be ca. 1.62 g/cm^3, which was lower than the density of the crystalline polymorphs of $CaCO_3$. By using time-resolved SAXS/WAXS, the transformation of ACC into microcrystals was observed in supersaturated solutions *in situ*. It was possible to detect the onset of particle dissolution by changes in the frequency of the oscillations in the scattered intensity typical of the spherical form factor (Fig. 5.4A), followed by the growth of crystalline $CaCO_3$ demonstrating itself as clear single diffraction peaks in the 2D WAXS pattern (Fig. 5.4B). By these means, it was deduced that crystalline polymorphs of $CaCO_3$ were formed from ACC via dissolution and subsequent heterogeneous nucleation of the crystals. Hence, the authors did not observe any solid–solid transition.

However, this latter transition from ACC to stable crystalline $CaCO_3$ phases has more recently been reevaluated also by simultaneous SAXS and WAXS (Bots et al., 2012; Rodriguez–Blanco, Bots, Roncal-Herrero, Shaw, & Benning, 2012; Rodriguez–Blanco et al., 2011). Using higher supersaturations compared to Bolze et al. (2002), Bots et al. (2012) showed that the crystallization of pure ACC to vaterite (μ-$CaCO_3$) proceeded via multiple stages but that the disappearance of the precipitated ACC particles, which were only 35–40 nm in diameter, occurred in less than 90 s (Fig. 5.5). These initial ACC nanoparticles dehydrated and dissolved and concomitantly vaterite formed via a nucleation-controlled mechanism. The data clearly showed that already after 2 min, vaterite nanocrystals, initially only ~9 nm in diameter, formed. In the next ~15 min, in a secondary stage, these individual nanocrystals grew to micron-sized spherulites. Noteworthy
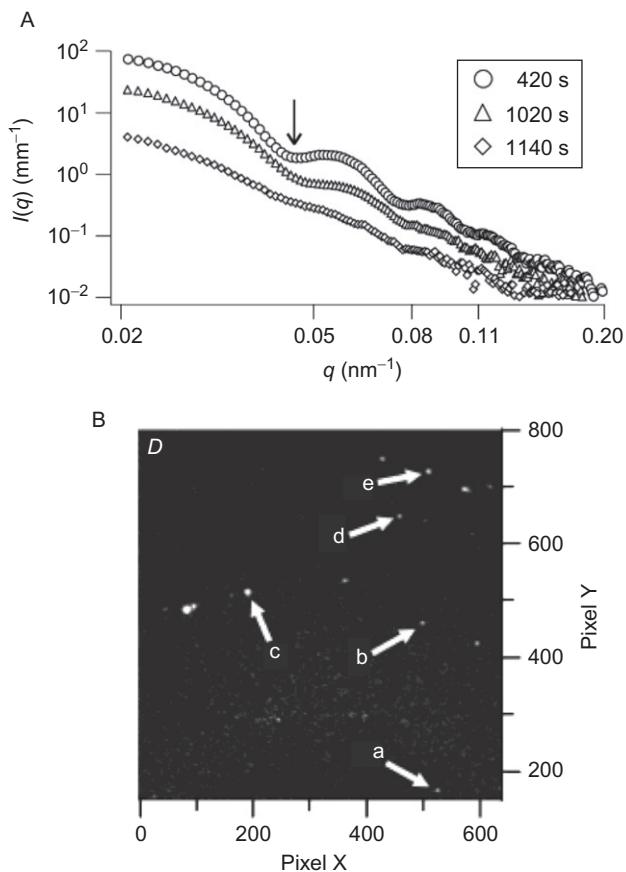
Figure 5.4 (A) SAXS curves after mixing reagent solutions for CaCO₃. The arrow indicates the first minimum of the spherical form factor. Its shift toward larger scattering angles indicates dissolution of the amorphous particles. The particles become more polydisperse, as suggested by the less pronounced oscillations in the scattering curve. The overall intensity decrease is due to particle dissolution and sedimentation. (B) WAXS pattern showing diffraction spots that can be assigned to the various crystalline metamorphs of calcium carbonate. The spots indicated by arrows correspond to the following Bragg reflections: (a) calcite (012), (b) vaterite (004), (c) aragonite (032), (d) aragonite (310), and (e) aragonite (302). *Printed with permission from Pontoni et al. (2003). Copyright 2003 American Chemical Society.*

however is the fact that each of these spherulites in turn was made up of individual nanoparticles that reached ∼60 nm in size. This intermediate stage of crystallization was rather short and in a subsequent stage the vaterite transformed to the stable calcite. This final reaction stage can, depending on temperature, last from a few to many hours (Rodriguez-Blanco et al., 2011)

and the vaterite spherulites transform to calcite, via a slower dissolution and reprecipitation mechanism. Interestingly, any change in parameters will also lead to a dramatic change in the crystallization pathway and mechanism. For example, the addition of magnesium leads to the direct transformation of ACC to calcite with no vaterite intermediate (Rodriguez-Blanco et al., 2012), while the addition of organics (e.g., ethanol, Sand, Rodriguez-Blanco, Makovicky, Benning, & Stipp, 2012) will stabilize aragonite instead of calcite (Fig. 5.5).

5.2. Nucleation and growth of silica nanoparticles

The mechanisms controlling silica precipitation are essential to the understanding of natural processes involving this material such as biosilicification (Konhauser, Jones, Phoenix, Ferris, & Renaut, 2004) but are also relevant to industrial applications when desired microstructure of silica is of crucial importance (Besselink et al., 2013; Brinker & Scherer, 1990; Iler, 1979). As a matter of fact, silica is probably one of the most intensively investigated by SAXS inorganic systems. Major concepts of clustering and aggregation, for example, mass-fractal aggregates (Freltoft et al., 1986; Teixeira, 1988), were experimentally derived and coined on the basis of silica-based systems. Nevertheless, in-depth studies about the nature and evolution of silica are in part still in their infancy. This is despite the fact that we desperately need this information in particular with a view towards improving our understanding of how the intricate biological shapes are created by living organisms (e.g., diatoms) as they control the global Si cycle in marine settings. Similarly, we need to understand how silica precipitates in geothermal systems and why and how to possibly prevent the clogging of pipes of heat exchangers in geothermal power plants in order to increase energy production.

In this worked example based on Tobler et al. (2009) and Tobler and Benning (2013), the nucleation and growth of silica nanoparticles was followed in aqueous solutions with initial silica concentrations of 640–1600 ppm, at different ionic strengths and at different temperatures. Silica polymerization and silica nanoparticle formation were induced either by adjusting the high-pH precursor solution to 7 or by inducing polymerization through an increase in supersaturation due to a fast temperature drop from 230 to 30–60 °C. SAXS scattering curves were collected for up to 3 h at a time resolution of 5 min/pattern. This was primarily because the electron density contrast between silica and aqueous solution was very low and longer time lengths were needed to improve a signal-to-noise ratio.
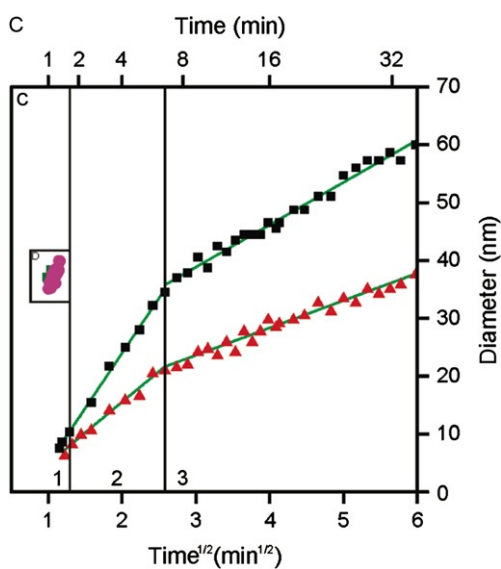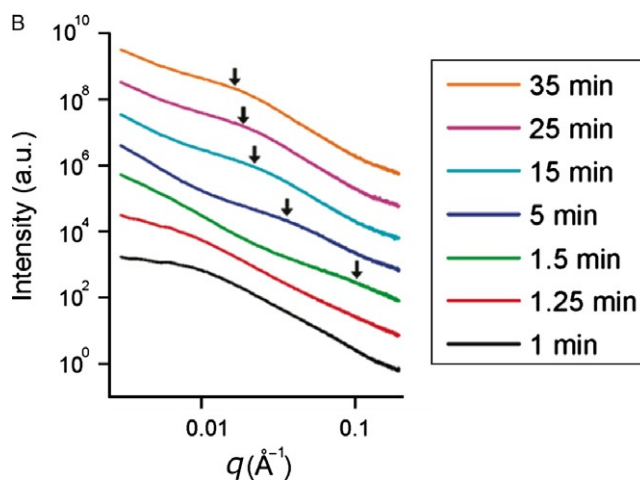
A

ACC

Time (s)

Vaterite

2 θ

Time (s)

B

Intensity (a.u.)

$q(\text{Å}^{-1})$

| 35 min |
| 25 min |
| 15 min |
| 5 min |
| 1.5 min |
| 1.25 min |
| 1 min |

C

Time (min)

Diameter (nm)
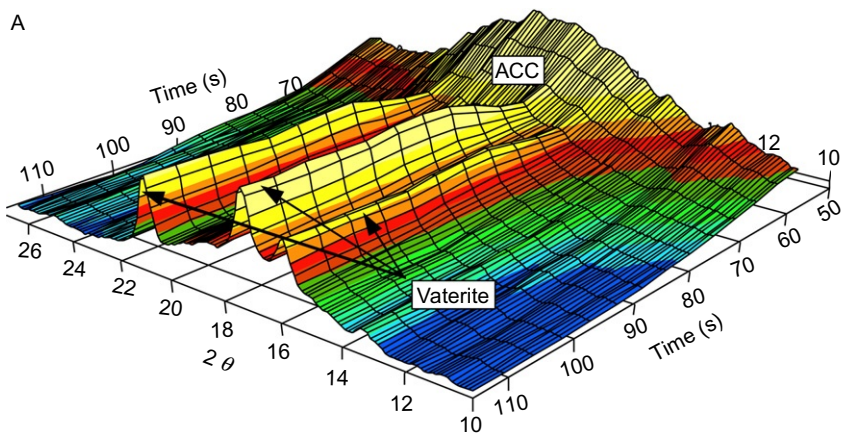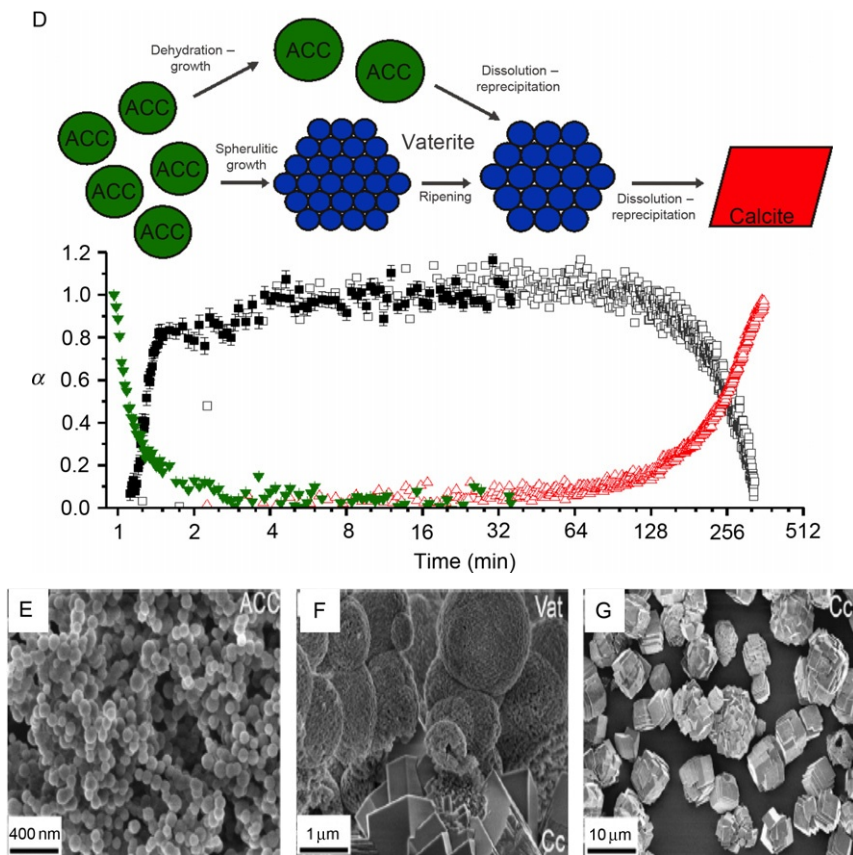
$\text{Time}^{1/2}(\text{min}^{1/2})$

Figure 5.5—Cont'd

Figure 5.5 (A) Three-dimensional representations of the time-resolved WAXS patterns from the pure ACC experiment (time is plotted on a base 2 log scale for clarity); (B) stacked time series of selected SAXS patterns from the pure ACC experiment, with the legend showing time in minutes and the arrows illustrating the position of the peaks caused by the scattering from the growing vaterite crystallites. (C) ACC nanoparticle and vaterite crystallite sizes derived from the SAXS data versus time (on a $t^{1/2}$ scale) for the pure ACC and an ACC doped with SO_4 experiments. (D) Schematic representation of the multistage ACC → vaterite → calcite crystallization pathway. (E–G) Electron microscope microphotographs of solids quenched throughout a full ACC to calcite transformation reaction. *Printed with permission from* Bots et al. (2012). *Copyright 2012 American Chemical Society.*

In Fig. 5.6A, a typical time-resolved SAXS curve from an experiment with one of the experimental solutions of SiO_2 is presented. The evolving system could practically, at all times, be treated as dilute, and the primary particles grew, but the interparticle interactions, such as aggregation, were practically negligible. These conclusions were drawn from the scattering curves where

A

B
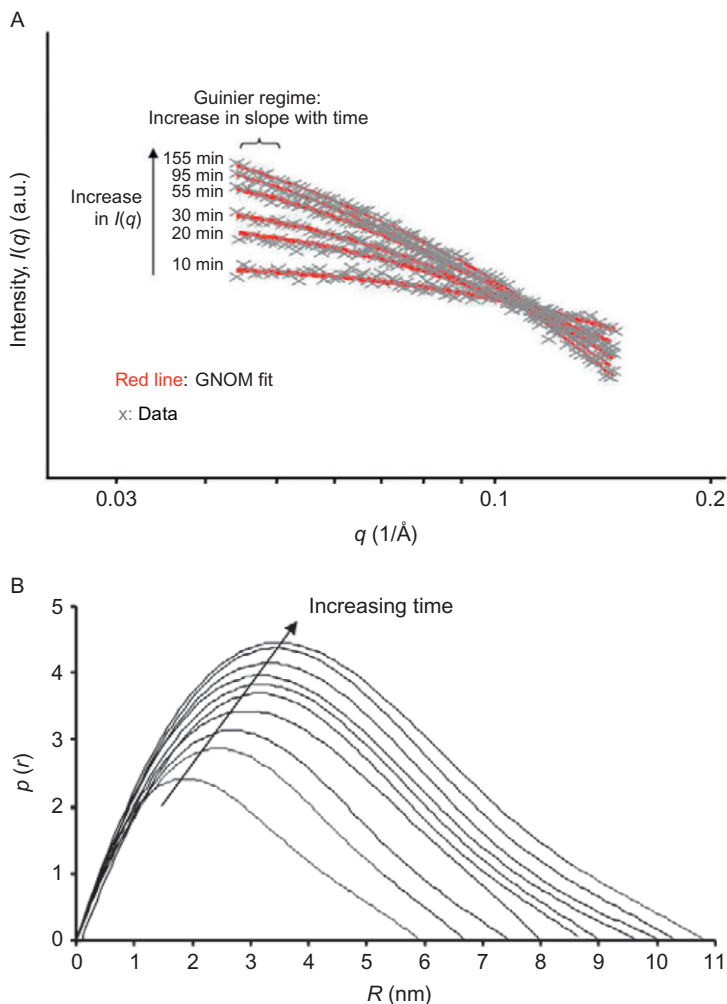
Figure 5.6 (A) $I(q)$ as a function of time for 640 ppm SiO_2. Solid lines depict GNOM fits; (B) pair distribution function plots, $p(r)$, of scattered silica nanoparticles as a function of r and time evaluated with GNOM. *Printed with permission from Tobler et al. (2009). Copyright 2009 Elsevier.*

two dominant features were present: (i) the overall increase in scattering intensity, $I(q)$ with time and (ii) the progressive shift of the scattering curves towards lower q in time. The increase in $I(q)$ was attributed to a change in electron density contrast between the matrix and the newly formed particles and a change in the total scattering volume of particles (i.e., increase in particle volume or number), whereas the shift of the scattering curves towards

lower q indicated an increase in the particles' sizes with time. Therefore, the cited example constitutes the case when $p(r)$ could be extracted from the scattering curves using the indirect Fourier transform methods, implemented, for example, in GNOM (Svergun, 1992). An example of a time-resolved distance distribution function, $p(r)$, for a polymerizing solution with 1600 ppm SiO_2 is shown in Fig. 5.6B. Over time, the $p(r)$ plot showed an increase in both the area under the curve and a shift in the apex of the curve indicating an increase in particle size. In the case of perfect, monodispersed spheres, the shape of each individual $p(r)$ curve should be Gaussian. Despite the $p(r)$ being slightly right-skewed, the near-Gaussian shape of the $p(r)$ curves obtained in this study suggested relatively low polydispersity of the system, although the actual distributions cannot be evaluated from these measurements due to the limited q-range. Hence, it was concluded that the observed tail could be induced by the presence of a few aggregates or it could also indicate the presence of some degree of polydispersity. The authors noted that the overall shape of the $p(r)$ curves did not differ between experiments (i.e., over the studied silica concentration, ionic strength, or temperature conditions), suggesting that the shape of the growing particles did not change between experiments. Electron microscopic evaluations using both conventional and cryoelectron microscopy verified the SAXS data and confirmed the spherical and hydrous structure of the forming silica nanoparticles. Information obtained from the SAXS patterns was further used to extract kinetic information about the process by fitting relevant kinetic models to the data. The results revealed that once polymerization was induced, a fast decrease in monomeric silica in solution was accompanied by a simultaneous increase in scattering intensity through the formation of silica nanoparticles with a $\sim$1–2 nm diameter. With time, these grew to reach a final size of about 7–8 nm. They showed that the nucleation and growth of silica nanoparticles from supersaturated solutions follows a three-stage process that proceeds through the homogenous and instantaneous nucleation of these initial nanoparticles followed by a 3D surface-controlled particle growth following a first-order reaction kinetics and in a latter step through Ostwald ripening and particle aggregation.

## 5.3. Evolution of the colloidal precursors for BaTiO$_3$

This example addresses the evolution of colloidal amorphous precursors for barium titanate also followed by time-resolved SAXS (Stawski et al., 2011a,2011b). BaTiO$_3$ is not a naturally occurring material, and it is derived

from alkoxides–carboxylate sol–gel process. This resembles in numerous aspects the previously described and well-studied similarly alkoxide-based formation of amorphous silica and again illustrates well the advantages and limitations of scattering methods. The $BaTiO_3$ precursor system is based on two components mixed together: titanium(IV) alkoxide dissolved in alcohol and barium acetate dissolved in acetic acid. Upon hydrolysis, initiated by water addition, sol particles of Ti(IV)oxo(hydroxo)acetate formed through condensation and further agglomeration resulting in an amorphous gel. The gelation process was attributed to the evolution of Ti-based phase and the formation of amorphous titania (TiO_x). Based on the SAXS and other complementary data sets (e.g., rheological characterization), the process could be derived into three growth stages: (i) formation of spherical primary Ti-(hydroxo)oxo clusters with an inorganic core diameter $2r_0 = 0.9$ nm and an outer organic ligand shell of ∼0.45 nm thickness, (ii) agglomeration of these primary particles into mainly mass-fractal-like agglomerates but with a minor component of correlated semiordered agglomerates, (iii) and cluster–cluster aggregation of structures from the previous phase into a 3D macroscopic gel of low density. The morphology and the kinetics of formation of the gel depended on initial hydrolysis conditions and the entire gelation process took between 0.5 and 3 h. The time-resolved scattering curves obtained from the *in situ* evolving system are presented in Fig. 5.7A.

The previously mentioned structural information was based on a scattering model developed to describe the precursor solution in terms of a mixture of mass-fractal-like agglomerates and structures with internal correlations, that is, semiordered agglomerates of similarly sized primary spherical particles. Both types of structures were composed of the same type of particles with a radius r_0 and a spherical form factor, $P(q)$. The fractal-like branched oligomeric structures were described using the mass-fractal structure $S_F(q)$ as defined in Freltoft et al. (1986), Sorensen (2001), and Teixeira (1988). The parameter D, the fractal dimension, can have values between 1 and 3, and this value relates the number of primary particles n of radius r_0 to its radius of gyration R_g. Therefore, a mass–fractal agglomerate fulfills the condition (Sorensen, 2001):

$$n \propto \left(\frac{R_g}{r_0} \right)^D \tag{5.11}$$

The second type of entities in solution was semiordered agglomerates of scatterers with similar size. These were described best by the hard-sphere
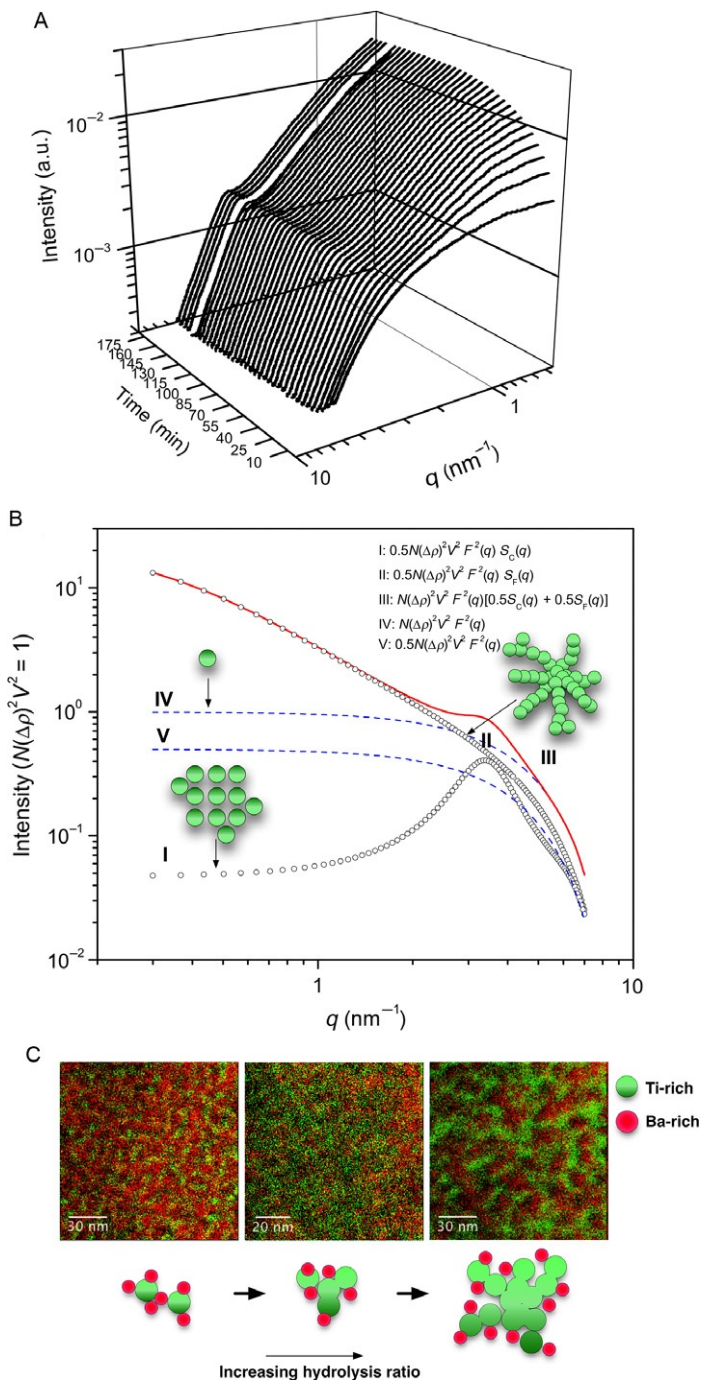
Figure 5.7 (A) Time-resolved SAXS patterns at 60 °C, showing evolution of barium titanate precursor sols of initial 0.5 mol/dm^3 concentration with hydrolysis ratio $[H_2O]/[Ti] = 5.6$. (B) Simulated SAXS curves using Eq. (5.12), with $N(\Delta\rho)^2 V^2$ set to 1.

(Continued)

Percus–Yevick structure factor $S_C(q)$ (Kinning & Thomas, 1984; Percus & Yevick, 1958) and depend on the hard–sphere radius R_{HS} (correlation radius) of the randomly packed spherical particles and their volume fraction v. The degree of ordering of such particles, located at a distance $2R_{HS}$ from each other, is expressed by v. To account for the fact that the relative contributions to scattering of the fractal and semiordered agglomerates in solution vary with time, a weighting factor $0 < \varepsilon < 1$ was introduced. This described the contribution of the fractal-like structures to the total scattering intensity. The scattering intensity from the sol upon gelation as the function of time was thus given by

$$I(q,t) = N(\Delta\rho)^2 P(q,t)\{\varepsilon(t)S_F(q,t) + [1-\varepsilon(t)]S_C(q,t)\} \qquad (5.12)$$

A few examples of scattering curves that were simulated using Eq. (5.12) are presented in Fig. 5.7B. The SAXS data as such did not indicate whether the emergent nanostructures were Ti- or Ba-related. This problem was overcome by juxtapositioning the results from SAXS with those from electron energy loss spectroscopy, (EELS) and energy-filtered transmission electron microscopy obtained from dried gel samples produced using various hydrolysis ratios (Fig. 5.7C). The resulting nanoscale resolution elemental maps allowed the authors demonstrate that processing of multicomponent amorphous precursors for barium titanate leads to spatially nonhomogenous structures resulting from the growth of amorphous titania only.

6. OUTLOOK

The previously described worked examples showing applications of SAXS in inorganic and bioinspired research and some of the examples contained in the references in this chapter cover only a miniscule fraction of SAXS knowledge base relevant to investigations related to the formation processes of inorganic phases from solution.

Figure 5.5—Cont'd (i) $I(q)$ of semiordered agglomerates with $r_0 = 0.5$ nm, $v = 0.3$, $2R_{HS} = 1.8$ nm, and $\varepsilon = 0.5$. (ii) $I(q)$ of fractal agglomerates with $r_0 = 0.5$ nm, $D = 1.8$, $R_g = 4.76$ nm, and $\varepsilon = 0.5$. (iii) $I(q)$ of linear combination of structures i and ii. (iv) $I(q)$ of sphere form factor of $r_0 = 0.5$ nm. (v) $I(q)$ of sphere form factor of $r_0 = 0.5$ nm and $\varepsilon = 0.5$. (C) EELS mappings of Ba (red) and Ti (green) of as-dried BTO films with increasing hydrolysis ratios. *Panels (A) and (B) are printed with permission from Stawski et al. (2011a) and panel (C) is printed with permission from Stawski et al. (2011b). Copyright 2011 American Chemical Society.*

The advances in detector technology in terms of acquisition accuracy, speed, and signal–to–noise levels now allow us to follow a process faster or at higher spatial resolution. This leads unfailingly to a dramatic increase in the amount of data acquired in each experiment. In addition, the higher quality of data that can now be achieved allows us to derive much more information from each data set. However, inconsistencies and limitations in data reduction and limited theoretical understanding of how we should or can process and/or model the resulting data sets are in many cases the bottleneck in our ability to quantitatively assess even simple solution–based nucleation and growth reactions. This is caused by the fact that existing theories of scattering do not handle well simultaneous contributions from different form factors, structure factor, and polydispersity. On the other hand, it should be stated that scattering methods are far more used and applied in fields such as polymer physics or protein structural biology. It is not an exaggeration if one says that the progress in our understanding of scattering, as well as development of data interpretation methods and theories, is due to the challenges in these two broad fields of interest. The inorganic scattering world in comparison is still in its infancy, yet advances in our theoretical understanding of nanoparticle interactions and how scattering data should be interpreted will lead to further advancement in the next decade. As long as scattering models developed in the other fields can be transferred to the solution–based nucleation and growth phenomena in inorganic systems, further progress in the data interpretation methods will also be essential. For example, one such advance is the use of reverse Monte Carlo modeling especially suited for disordered systems. Such approaches open up new possibilities in SAXS data interpretation in combination with WAXS and XAS (McGreevy & Pusztai, 1988).

In fact, electron microscopy is the most powerful ally of SAXS. For example, by using cryoquench TEM, one can obtain information from different stages of the synthesis reaction by cryoquenching of samples, which allows to look at various time–resolved "snapshots" of the reaction. With this approach, samples in their liquid state are rapidly (<1 s) cryoquenched and flash-frozen and subsequently imaged in cryomode at high resolution. Such cryoimaging of developing structures is a major first step in understanding reactions at high resolution and these are highly complementary to any SAXS or WAXS data sets. However, one of the most exciting recent developments is a liquid–cell system for TEM/STEM, where the self–assembly of the forming structures can be followed *in situ* (Li et al., 2012; Liao, Cul, Whitelam, & Zheng, 2012). In conventional electron microscopy, samples

are usually exposed to very high vacuum, completely removing the solvent environment, while in cryoquenched systems, a continuous process cannot be followed. Rapid drying or cryoquenching often leads to artifacts, and this hinders the direct data correlation with the other measurements in which the solvent environment is preserved (i.e., SAXS/WAXS). Using a liquid-cell system in conjunction with the high-resolution imaging allows us to characterize the dynamics and progress of reactions at the nanoscale but with the samples still in the fluid phase. In such a TEM fluid cell, a droplet of the reacting liquid sample is sealed between two electron-transparent membranes. This allows for quantitative and qualitative image and spectral analyses of the nucleation, crystallization, self-assembly, and agglomeration processes of inorganic phases at an unprecedented resolution and in a most direct manner. This way, a direct link between *in situ* TEM imaging and scattering data from *in situ* synchrotron–based SAXS/WAXS is warranted.

ACKNOWLEDGMENTS

REFERENCES

Ahmed, I. A. M., Benning, L. G., Kakonyi, G., Sumoondur, A., Terrill, N. J., & Shaw, S. (2010). The formation of green rust sulfate: Situ and time-resolved scattering and electrochemistry. *Langmuir, 26*(9), 6593–6603.

Baumgartner, J., Dey, A., Bomans, P. H. H., Le Coadou, C., Fratzl, P., Sommerdijk, N. A. J. M., et al. (2013). Nucleation and growth of magnetite from solution. *Nature Materials, 12*, 310–314.

Becker, D., & Döring, W. (1935). The kinetic treatment of nuclear formation in supersaturated vapors. *Annalen der Physik, 24*, 719–752.

Benning, L. G., & Waychunas, G. (2007). Nucleation, growth, and aggregation of mineral phases: Mechanisms and kinetic controls. In S. L. Brantley, J. D. Kubicki, & A. F. White (Eds.), *Kinetics of water-rock interaction*.New York: Springer-Verlag, chapter 7.

Besselink, R., Stawski, T. M., Castricum, H. L., & ten Elshof, J. E. (2013). Evolution of microstructure in mixed niobia-hybrid silica thin films from sol–gel precursors. *Journal of Colloid and Interface Science, 404*, 24–35.

Bolze, J., Peng, B., Dingenouts, N., Panine, P., Narayanan, T., & Ballauff, M. (2002). Formation and growth of amorphous colloidal $CaCO_3$ precursor particles as detected by time-resolved SAXS. *Langmuir, 18*, 8364–8369.

Bots, P., Benning, L. G., Rodriguez-Blanco, J.-D., Roncai-Herrero, T., & Shaw, S. (2012). Mechanistic insights into the crystallization of amorphous calcium carbonate (ACC). *Crystal Growth and Design, 12*(7), 3806–3814.

Brand, H. E. A., Scarlett, N. V. Y., Grey, I. E., Knott, R. B., & Kirby, N. (2013). In situ SAXS studies of the formation of sodium jarosite. *Journal of Synchrotron Radiation, 20*(4), 626–634.

Bras, W. (1998). An SAX/WAXS beamline at the ESRF and future experiments. *Journal of Macromolecular Science, Part B: Physics*, *37*(4), 557–565.

Brinker, C. J., & Scherer, G. W. (1990). *Sol-gel: The physics and chemistry of sol-gel processing.* London: Academic Press.

Brunner-Popela, J., & Glatter, O. (1997). Small-angle scattering of interacting particles. I. Basic principles of a global evaluation technique. *Journal of Applied Crystallography*, *30*(4), 431–442.

Cahill, C. L., Benning, L. G., Barnes, H. L., & Parise, J. B. (2000). In situ time-resolved X-ray diffraction of iron sulfides during hydrothermal pyrite growth. *Chemical Geology*, *167*(1–2), 53–63.

Craievich, A. F. (2002). Synchrotron SAXS studies of nanostructured materials and colloidal solutions. A review. *Materials Research*, *5*(1), 1–11.

Davidson, L. E., Shaw, S., & Benning, L. G. (2008). The kinetics and mechanisms of schwertmannite transformation to goethite and hematite under alkaline conditions. *American Mineralogist*, *93*, 1326–1337.

Dey, A., Bomans, P. H. H., Müller, F. A., Will, J., Frederik, P. M., de With, G., et al. (2010). The role of prenucleation clusters in surface-induced calcium phosphate crystallization. *Nature Materials*, *9*, 1010–1014.

Feigin, L. A., & Svergun, D. I. (1987). *Structure analysis by small-angle X-ray and neutron scattering.* New York and London: Plenum Press.

Fratzl, P., Misof, K., Zizak, I., Rapp, G., Amenitsch, H., & Bernstorff, S. (1997). Fibrillar structure and mechanical properties of collagen. *Journal of Structural Biology*, *122*(1–2), 119–122.

Freltoft, T., Kjems, J. K., & Sinha, S. K. (1986). Power-law correlations and finite-size effects in silica particle aggregates studied by small-angle neutron scattering. *Physical Review B*, *33*, 269–275.

Gebauer, D., & Cölfen, H. (2011). Prenucleation clusters and non-classical nucleation. *Nano Today*, *6*, 564–584.

Gebauer, D., Völkel, A., & Cölfen, H. (2008). Stable prenucleation calcium carbonate clusters. *Science*, *322*(5909), 1819–1822.

Glatter, O. (1977). A new method for the evaluation of small-angle scattering data. *Journal of Applied Crystallography*, *10*(5), 415–421.

Glatter, O. (1981). Convolution square root of band-limited symmetrical functions and its application to small-angle scattering data. *Journal of Applied Crystallography*, *12*(2), 101–108.

Glatter, O., & Kratky, O. (Eds.), (1982). *Small angle X-ray scattering.* London: Academic Press.

Gower, L. B. (2008). Biomimetic model systems for investigating the amorphous precursor pathway and its role in biomineralization. *Chemical Reviews*, *108*, 4551–4627.

Guinier, A., & Fournet, G. (1955). *Small angle scattering of X-rays.* New York: John Wiley & Sons Inc.

Huang, T. C., Toraya, H., Blanton, T. N., & Wu, Y. (1993). X-ray powder diffraction analysis of silver behenate, a possible low-angle diffraction standard. *Journal of Applied Crystallography*, *26*(2), 180–184.

Hunger, S., & Benning, L. G. (2007). Greigite: The intermediate phase on the pyrite formation pathway. *Geochemical Transactions*, *8*(1), 1–20.

Iler, R. K. (1979). *The chemistry of silica.* New York: John Wiley & Sons.

Jalava, J.-H., Hiltunen, E., Kähkönen, H., Erkkilä, H., Härmä, H., & Taavitsainen, V.-M. (2000). Structural investigation of hydrous titanium dioxide precipitates and their formation by small-angle X-ray scattering. *Industrial & Engineering Chemistry Research*, *39*, 349–361.

Kamiyama, T., Mikami, M., & Suzuki, K. (1992). A SAXS study of the gelation process of silicon and titanium alkoxides. *Journal of Non-Crystalline Solids*, *150*, 157–162.

Kinning, D. J., & Thomas, E. L. (1984). Hard-sphere interactions between spherical domains in diblock copolymers. *Macromolecules*, *17*, 1712–1718.

Konhauser, K. O., Jones, B., Phoenix, V. R., Ferris, F. G., & Renaut, R. W. (2004). The microbial role in hot spring silicification. *Ambio*, *33*, 552–558.

Li, D., Nielsen, M. H., Lee, J. R. I., Frandsen, C., Banfield, J. F., & De Yoreo, J. J. (2012). Direction-specific interactions control crystal growth attachment. *Science*, *336*, 1014–1018.

Liao, H.-G., Cul, L., Whitelam, S., & Zheng, H. (2012). Real-time imaging of Pt_3Fe nanorod growth in solution. *Science*, *336*, 1011–1014.

Loste, E., Wilson, R. M., Seshadri, R., & Medrum, F. C. (2003). The role of magnesium in stabilizing amorphous calcium carbonate and controlling calcite morphologies. *Journal of Crystal Growth*, *254*, 206–218.

McGreevy, R. L., & Pusztai, L. (1988). Reverse Monte Carlo simulation: A new technique for the determination of disordered structures. *Molecular Simulation*, *1*(6), 359–367.

Meldrum, F. C., & Cölfen, H. (2008). Controlling mineral morphologies and structures in biological and synthetic system. *Chemical Reviews*, *108*, 4332–4432.

Meldrum, F. C., & Sear, R. P. (2008). Now you see them. *Science*, *322*, 1802–1803.

Mueller, M., Wang, M., & Schulze-Briese, C. (2012). Optimal fine φ-slicing for single-photon-counting pixel detectors. *Acta Crystallographica Section D: Biological Crystallography*, *D68*, 42–56.

Pauw, B. R. (2013). Everything SAXS: small-angle scattering pattern collection and correction. *Journal of Physics: Condensed Matter*, *25*, 383201 (24pp).

Pedersen, J. K. (1997). Analysis of small-angle scattering data from colloids and polymer solutions: Modelling and least-squares fitting. *Advances in Colloid and Interface Science*, *70*, 171–210.

Percus, J. K., & Yevick, G. J. (1958). Analysis of classical statistical mechanics by means of collective coordinates. *Physical Review*, *110*, 1–13.

Polte, J., Erler, R., Thünermann, A. F., Sokolov, S., Ahner, T. T., Rademannm, K., et al. (2010). Nucleation and growth of gold nanoparticles studied via in situ small angle X-ray scattering at millisecond time resolution. *ACS Nano*, *4*(2), 1076–1082.

Pontoni, D., Bolze, J., Dingenouts, N., Narayanan, T., & Ballauff, M. (2003). Crystallization of calcium carbonate observed in-situ by combined small- and wide-angle X-ray scattering. *The Journal of Physical Chemistry, B*, *107*, 5123–5125.

Putnam, C. D., Hammel, M., Hura, G. L., & Tainer, J. A. (2007). X-ray solution scattering (SAXS) combined with crystallography and computation: Defining accurate macromolecular structures, conformations and assemblies in solution. *Quarterly Reviews of Biophysics*, *40*(3), 191–285.

Rieckel, C., Burghammer, M., & Müller, M. (2000). Microbeam small-angle scattering experiments and their combination with microdiffraction. *Journal of Applied Crystallography*, *33*, 421–423.

Riello, P., Minesso, A., Craievich, A., & Benedetti, A. (2003). Synchrotron SAXS study of the mechanisms of aggregation of sulfate zirconia sols. *The Journal of Physical Chemistry B*, *107*(15), 3390–3399.

Rodriguez-Blanco, J.-D., Bots, P., Roncal-Herrero, T., Shaw, S., & Benning, L. G. (2012). The role of pH and Mg on the stability and crystallization of amorphous calcium carbonate. *Journal of Alloys and Compounds*, *536*(S1), S477–S479.

Rodriguez-Blanco, J.-D., Shaw, S., & Benning, L. G. (2008). How to make stable ACC: Protocol and structural characterization. *Mineralogical Magazine*, *72*(1), 283–286.

Rodriguez-Blanco, J.-D., Shaw, S., & Benning, L. G. (2011). The kinetics and mechanisms of amorphous calcium carbonate (ACC) crystallization to calcite, via vaterite. *Nanoscale*, *3*, 265–271.

Sand, K. K., Rodriguez-Blanco, J.-D., Makovicky, E., Benning, L. G., & Stipp, S. S. L. (2012). Crystallization of CaCO3 in water/alcohol mixtures: Spherulitic growth, polymorph stabilization and morphology change. *Crystal Growth and Design*, *12*(2), 842–853.

Sorensen, C. M. (2001). Light scattering by fractal aggregates: A review. *Aerosol Science and Technology*, *35*, 648–687.

Squires, G. L. (1978). *Introduction to the theory of thermal neutron scattering*. Cambridge: Cambridge University Press.

Stawski, T. M., Besselink, R., Veldhuis, S. A., Castricum, H. L., Blank, D. H. A., & ten Elshof, J. E. (2012). Time-resolved small angle X-ray scattering study of sol–gel precursor solutions of lead zirconate titanate and zirconia. *Journal of Colloid and Interface Science*, *369*, 184–192.

Stawski, T. M., Veldhuis, S. A., Besselink, R., Castricum, H. L., Portale, G., Blank, D. H. A., et al. (2011a). Nanoscale structure evolution in alkoxide-carboxylate sol–gel precursor solutions of barium titanate. *The Journal of Physical Chemistry C, 115*(42), 20449–20459, Correction to nanoscale structure evolution in alkoxide-carboxylate sol–gel precursor solutions of barium titanate. The Journal of Physical Chemistry C, 115, 24028-24028.

Stawski, T. M., Veldhuis, S. A., Besselink, R., Castricum, H. L., Portale, G., Blank, D. H. A., et al. (2011b). Nanostructure development in alkoxide-carboxylate-derived precursor films of barium titanate. *The Journal of Physical Chemistry C, 116*(1), 425–434.

Stawski, T. M., Veldhuis, S. A., Castricum, H. L., Keim, E. G., Eeckhaut, G., Bras, W., et al. (2011). Development of nanoscale inhomogeneities during drying of sol-gel derived amorphous lead zirconate titanate precursor thin films. *Langmuir*, *27*(17), 11081–11089.

Stribeck, N. (2007). *X-ray scattering of soft matter.* Berlin, Heidelberg, New York: Springer.

Sumoondur, A., Shaw, S., Ahmed, I., & Benning, L. G. (2008). Green rust a precursor for magnetite: An in situ synchrotron based study. *Mineralogical Magazine*, *72*(1), 201–204.

Svergun, D. I. (1992). Determination of the regularization parameter in indirect-transform methods using perceptual criteria. *Journal of Applied Crystallography*, *25*(4), 495–503.

Teixeira, J. (1988). Small-angle scattering by fractal systems. *Journal of Applied Crystallography*, *21*(6), 781–785.

Tobler, D. J., & Benning, L. G. (2013). The in situ and time resolved nucleation and growth of silica nanoparticles under simulated geothermal conditions. *Geochimica et Cosmochimica Acta*, *144*, 156–168.

Tobler, D. J., Shaw, S., & Benning, L. G. (2009). Quantification of initial steps of nucleation and growth of silica nanoparticles. An in-situ SAXS and DLS study. *Geochimica et Cosmochimica Acta*, *73*(18), 5377–5393.

Vachette, P., & Svergun, D. I. (2000). Small-angle X-ray scattering by solutions of biological macromolecules. In E. Fanchon, G. Geissler, J.-L. Hodeau, J.-R. Regnard, & P. A. Timmins (Eds.), *Structure and dynamics of biomolecules*.New York: Oxford University Press, Chapter 11.

Volmer, M., & Weber, A. (1925). Keimbildung in übersättigten Gebilden. *Zeitschrift für Physikalische Chemie*, *119*, 277–301.

Vu, H. P., Shaw, S., Brinza, L., & Benning, L. G. (2010). Crystallization of hematite (alpha-Fe_2O_3) under alkaline condition: The effects of Pb. *Crystal Growth and Design*, *10*(4), 1544–1551.

Wright, J. D., & Sommerdijk, N. A. J. M. (2001). *Sol-gel materials chemistry and applications. Advanced chemistry texts*Boca Raton: CRC Press.